Materials Advances

ROYAL SOCIETY OF CHEMISTRY

PAPER

View Article Online
View Journal | View Issue

Cite this: *Mater. Adv.*, 2026, 7, 2874

Atomic layer deposition of gallium oxide using gallium triazenide and water

Prosper Simbarashe Mushore,[a] Pamburayi Mpofu,[a] Kenichiro Mizohata,[b] Kostas Sarakinos,[bc] Nathan J. O'Brien[a] and Henrik Pedersen[*a]

Gallium oxide (Ga_2O_3) is an ultrawide bandgap semiconductor with promising applications in power electronics and UV-photodetectors. Herein, we present thermal atomic layer deposition (ALD) of Ga_2O_3 thin films using tris(1,3-diisopropyltriazenide)gallium(III) and water. The deposition process shows saturation in the growth per cycle of ~1.5 Å at precursor pulses ≥2 s with a narrow ALD temperature interval between 400 and 415 °C, and a nucleation delay of ~15 cycles. Time-of-flight elastic recoil detection analysis revealed near-stoichiometric Ga_2O_3 with <3.5 at%, of C, H, N, and Cl, all of which decreases after annealing. Grazing Incidence X-ray diffraction reveals that annealing at 700 °C converts as-deposited amorphous films into phase-pure β-Ga_2O_3. The as-deposited films were highly transparent (>96%) with an optical bandgap of ~3.74 eV, which increased to ~4.0 eV upon annealing. Electrical conductivity also increased from ~3 mS cm^{-1} in the as deposited films to ~30 mS cm^{-1} after annealing. This work extends the ALD chemistry of triazenide precursors, previously validated for GaN, InN, InGaN and In_2O_3, to Ga_2O_3.

Received 21st October 2025,
Accepted 2nd February 2026

DOI: 10.1039/d5ma01213a

rsc.li/materials-advances

1. Introduction

Wide-bandgap (WBG) semiconductors provide orders-of-magnitude higher breakdown fields and lower carrier leakage than Si.[1] Breakthroughs in the 1990s–2000s, notably with silicon carbide (SiC) and gallium nitride (GaN), enabled high-voltage Schottky diodes, metal-oxide-semiconductor field-effect transistors (MOSFETs) and high-electron-mobility transistors (HEMTs), all of which are now widely used in electric-vehicle inverters, server power supplies, and radio-frequency amplifiers.[2] Over the past decade, attention has shifted to ultra-wide-bandgap (UWBG) materials (bandgaps >4 eV), because they promise greater performance gains.[3] This subclass includes β-gallium oxide (β-Ga_2O_3), diamond, and aluminium nitride.[4] The wider bandgaps of WBG and UWBG semiconductors, relative to Si, yield exponentially lower intrinsic carrier concentrations, and enable high-temperature operation.[5] Their high critical breakdown fields also allow devices to block high voltages with thinner, more heavily doped drift layers, dramatically reducing on-state losses.[6] Direct-bandgap UWBG materials are strongly transparent in the deep UV-region, making them suitable for solar-blind photodetectors and other related optical devices.[7] β-Ga_2O_3 has an optical bandgap of 4.8 eV (absorption edge ≈255 nm),[7] rendering it solar-blind (insensitive above ~280 nm) and attractive for UV photodetectors and optical coatings. Stoichiometric, highly pure β-Ga_2O_3 films are typically clear and highly transparent, however, O-vacancies and impurities can impart yellowish or bluish tints.[8] The ability to tune these optical features by controlling film composition is advantageous for UV-sensor and filter applications.

Ga_2O_3 crystallizes in five polymorphs - α, β, γ, δ, and ε (κ), and among these β-Ga_2O_3, with a monoclinic *C*2/*m* structure, is the most thermodynamically stable phase at ambient pressure. The remaining polymorphs are metastable and convert irreversibly to the β-phase upon annealing.[9] Notably, α-Ga_2O_3 offers the widest bandgap (~5.2 eV), while the ε- (κ-) phase is of interest for its ferroelectric behaviour and potential for polarization-engineered devices.[8,10]

Thin-film deposition is crucial for semiconductor fabrication, as it enables nanoscale layers of metals, insulators, and semiconductors to be formed on various substrates.[11] A common thin-film deposition technique in the semiconductor field is chemical vapor deposition (CVD), where volatile molecules react in the gas phase and on the surface to deposit the atoms that form the film.[12] Atomic layer deposition (ALD) is a time-resolved form of CVD that achieves atomic-scale film growth by using sequential, self-limiting surface reactions.[13] In ALD, the precursors, *e.g.*, Ga and O, are introduced separately and

[a] *Department of Physics, Chemistry, and Biology, Linköping University, SE-581 83 Linköping, Sweden. E-mail: henrik.pedersen@liu.se*
[b] *Department of Physics, University of Helsinki, P.O. Box 43, Helsinki, FI-00014, Finland*
[c] *KTH Royal Institute of Technology, Department of Physics, Roslagstullsbacken 21, 114 21 Stockholm, Sweden*

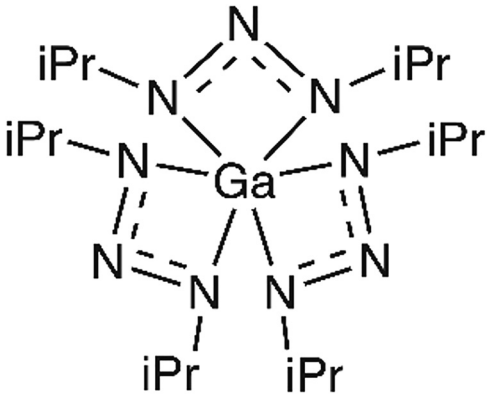

Fig. 1 Structure of the previously reported (Ga(triaz)$_3$) precursor (ref. 22).

isolated in time by inert-gas purges, thus preventing any gas-phase reactions. ALD offers several advantages that make it particularly attractive for advanced semiconductor device fabrication. Most notably, it provides atomic-scale thickness control since the thickness is governed solely by the number of ALD cycles. Ideally, the self-limiting surface reactions ensure excellent conformality, even over complex 3D nanostructures. ALD also enables low-temperature deposition, with many thermal-ALD temperature intervals for metal-oxide systems lying below 350 °C, much lower than typical CVD temperatures.

ALD of Ga_2O_3 with water as the O precursor has been reported using Ga alkyl ($Ga(CH_3)_3$),[14] halide ($GaCl_3$),[15] alkylamide ($Ga(N(CH_3)_2)_3$),[16] β-diketonate ($Ga(acac)_3$),[17] isopropoxide ($Ga(^iOC_3H_8)_3$),[18] and heteroleptic ($(CH_3)_2Ga^iOC_3H_8$)[19] precursors. We have recently explored a new ligand family, 1,3-dialkyltriazenides (R–N═N–N–R), for ALD of nitrides and oxides, and reported the synthesis and volatility of triazenide complexes with several metals in groups 11 to 14 of the periodic table.[20] To date, ALD has only been shown using tris(1,3-diisopropyltriazenide)indium(III) ($In(triaz)_3$) and tris(1,3-diisopropyltriazenide)gallium(III) ($Ga(triaz)_3$) precursors. Using NH_3 plasma as the N-source, $In(triaz)_3$ and $Ga(triaz)_3$ (Fig. 1) enabled ALD of high-quality InN[21] and GaN.[22] A mixture of $In(triaz)_3$ and $Ga(triaz)_3$, co-sublimed into the ALD reactor, facilitated ALD of $In_{1-x}Ga_xN$ using NH_3 plasma, with the In content widely tunable.[23] $In(triaz)_3$ has also been shown to deposit In_2O_3 by ALD with water as O-source.[24] Herein, we explore thermal ALD of Ga_2O_3 using $Ga(triaz)_3$, with water in an effort to expand the understanding of the triazenide ligand system for ALD.

2. Experimental details

2.1. Film deposition

$Ga(triaz)_3$ was synthesized according to previously reported procedures.[22,25] Films were deposited using a home-built cross-flow ALD reactor at 50 hPa. A flow of N_2 (99.999%) was used as the carrier and purging gas. During deposition, the N_2 pressure was held constant. Prior to deposition, p-type Si(100) wafers were cut and sequentially sonicated for five minutes each in acetone, isopropyl alcohol, and deionized water, followed by drying under a high-purity N_2 jet. Thus the Si substrates had a natural oxide layer. In some experiments, films were deposited on glass substrates, cleaned by the same procedure. The cleaned substrates were secured to a stainless-steel holder using Cu wire and loaded into the ALD reactor. The reactor and substrates were baked overnight at 200 °C to remove any adsorbates.

In an N_2 glovebox, ~0.5 g of $Ga(triaz)_3$ was transferred to a stainless-steel bubbler and mounted on the ALD system. During deposition, the bubbler was held at 160 °C and all delivery lines were heated at 170–180 °C. Water vapor was supplied from a room-temperature deionized water bubbler. Given the vapor pressure of water at 25 °C (~23 Torr), no additional carrier gas was required. The substrate stage was maintained at 400 °C during deposition unless noted otherwise. After optimization, a typical ALD cycle consisted of a 2 s $Ga(triaz)_3$ pulse, a 10 s N_2 purge, a 2 s water pulse, and a 10 s N_2 purge. These settings were used unless otherwise noted.

2.2. Film characterization

Elemental analysis of the film was carried out with time-of-flight elastic recoil detection analysis (ToF-ERDA). Data were collected on the EGP-10-II 5 MV tandem accelerator at the Helsinki Accelerator Laboratory.[26] Measurements were performed using a 40 MeV $^{127}I^{7+}$ ion beam, with the detector positioned at 40° relative to the incident beam, while the beam incident direction formed an angle of 20° relative to the sample surface. Composition and depth profiles were calculated using stopping forces obtained from the SRIM software,[27] the measurement geometry, and Rutherford elastic-recoil cross sections for the detected elements.

Crystallographic structure and phase formation were assessed using grazing-incidence X-ray diffraction (GI-XRD), while film thickness was determined by complementary X-ray reflectivity (XRR). Both GI-XRD and XRR were performed using a PANalytical X'Pert PRO equipped with a Cu Kα radiation source (λ = 1.5418 Å). For GI-XRD, the incident angle was fixed at 0.5°, and the 2θ range was 20°–70° at a step size of 0.2° and a dwell time of 1 s per step. XRR used parallel beam optics and reflectivity curves were analysed using the PANalytical X'Pert Reflectivity software[28] employing model-based fitting with the Parratt formalism to extract film thickness.

Surface morphology was examined using high-resolution scanning electron microscopy (SEM). An accelerating voltage of 3 kV was used to enhance surface sensitivity while minimizing sample charging. A working distance of 3–4 mm was maintained to optimize resolution with the in-lens secondary electron detector, enabling high-contrast imaging of surface features. To study thermal effects on film properties, annealing was carried out under controlled conditions. Films deposited on Si substrates were annealed at 700 °C for 2 h under N_2 or ambient air. Films deposited on glass substrates were annealed at 500 °C for 4 h under ambient air.

A Shimadzu UV-2600i spectrophotometer was used to measure the UV-vis transmittance of thin films deposited on glass

substrates, both in their as-deposited and post-annealed states at 500 °C for 4 h in ambient air. Transmittance spectra were recorded for the uncoated glass substrate (reference) and the Ga_2O_3-coated samples, and the data were normalized by dividing the sample intensity by the reference. The wavelength range was 300–800 nm, with a sampling interval of 1 nm. All measurements were conducted at room temperature. The processed data were used to compute absorbance, absorption coefficient (α), and optical bandgap *via* Tauc-plot analysis. Sheet resistance measurements were performed using a Jandel RM3000 four-point probe system, consisting of a digital control unit and a manual spring-loaded probe head. Measurements were conducted at room temperature under ambient conditions. Multiple measurements were taken across each sample to assess homogeneity and reproducibility. Film thickness was obtained from XRR measurements and used in the calculation of electrical conductivity.

3. Results and discussion

3.1. Film deposition

The dependence of growth-per-cycle (GPC) on precursor pulse length is shown in Fig. 2 for both $Ga(triaz)_3$ and water pulses during the ALD process at 400 °C. The observed trends show self-limiting behaviour. For very short pulses (0–2 s), the GPC increases sharply with pulse length for both precursors, indicating progressive occupation of surface reactive sites. For pulse lengths $\geq$2 s, the GPC plateaus at $\sim$1.5 Å per cycle for both precursors, consistent with a self-limited growth regime. The observed GPC is comparable to other reported ALD processes for Ga_2O_3; a Ga alkoxide process that saturated at 2.5 Å per cycle,[18] and a Ga dialkylamine process that saturated at 1.8 Å per cycle.[16]

Film growth over a broad temperature range (200–500 °C) was observed only within 395–420 °C. The GPC *versus* deposition temperature across this active interval is plotted in Fig. 3. The GPC increases from 1.1 Å per cycle at 395 °C to 1.5 Å per cycle at 400 °C, followed by a nearly constant value up to 415 °C, indicative of a stable, self-limiting reaction regime. At 420 °C, the GPC drops sharply to 0.6 Å per cycle, suggesting a departure from ideal ALD behaviour. We hypothesise that insufficient activation of surface reactions limits growth below 395 °C. Above 420 °C, reduced surface residence time of the precursor, due to desorption or accelerated surface decomposition, supresses growth. This ALD temperature interval is similar to that reported previously for GaN using the same Ga precursor.[22] Although the onset decomposition of the precursor has been speculated to be around 350 °C,[22] effective delivery and self-limited growth are still realised between 395–415 °C under our reactor conditions. It has also been proposed that the triazenide ligand can thermally decompose to a less bulky isopropylamine ligand which constitutes the surface-active intermediate.[21] We see no reason why this proposed mechanism should not be active also in this process.

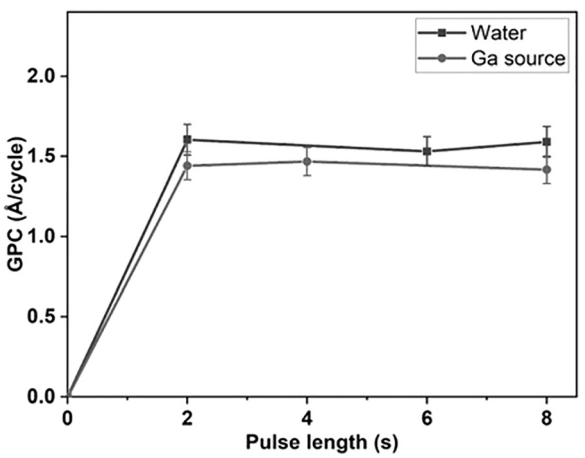

Fig. 2 GPC as a function of precursor pulse length for $Ga(triaz)_3$ (grey circles) and water (black squares) during ALD at 400 °C. When varying the pulse length of one precursor, the other was held constant at 8 s (*i.e.* water = 8 s when $Ga(triaz)_3$, was varied, and $Ga(triaz)_3$ = 8 s when water was varied).

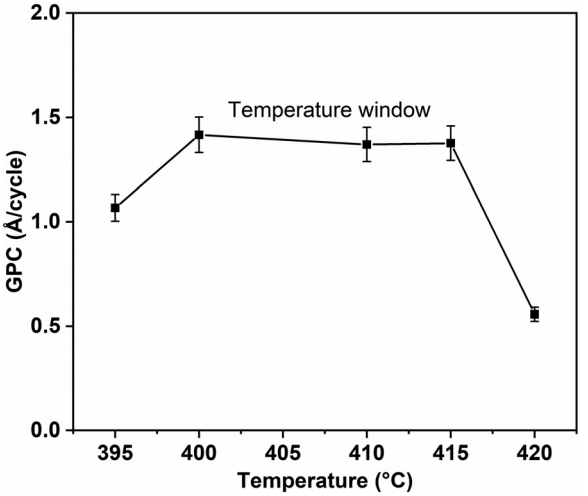

Fig. 3 GPC as a function of temperature. Measurable film growth was observed between 395–420 °C, with a narrow ALD interval identified between 400–415 °C where GPC remains approximately constant. ALD cycles used 8 s pulses for both $Ga(triaz)_3$ and water, separated by 10 s purges; all films were deposited for 300 cycles.

Compared to established Ga precursors, the thermal ALD process developed here exhibits a narrow, relatively high-temperature interval (400–415 °C). This behaviour is consistent with the low reactivity of water and the steric hindrance of the triazenide ligand, both of which can impede surface reactivity and require higher temperatures for complete ligand elimination. In contrast, plasma ALD processes, particularly those employing O_2 plasma, typically operate at much lower temperatures (60–250 °C) and show improved reactivity due to the generation of highly energetic species. For example, plasma ALD of Ga_2O_3 using $Ga_2(NMe_2)_6$ achieves GPCs of 1.4–1.6 Å per cycle at 60–160 °C,[29] while $Ga(CpMe_5)$ combined with water and O_2 plasma reaches 0.6 Å per cycle between 150–250 °C.[30] $Ga(CH_3)_3$ also benefits from plasma activation, with GPCs of 0.53 Å per cycle reported across a wide temperature interval

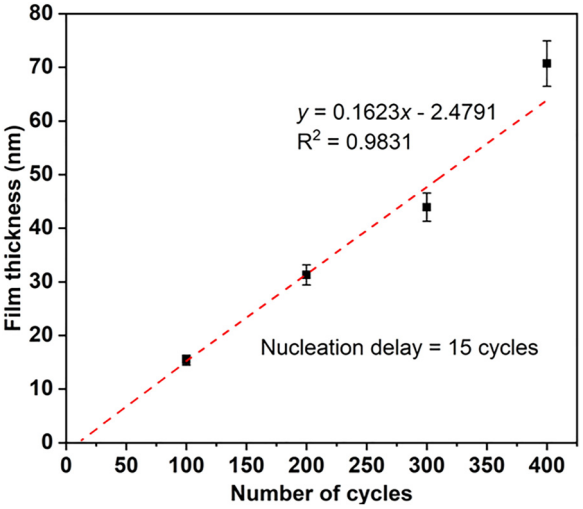

Fig. 4 Film thickness *versus* number of ALD cycles for Ga_2O_3 on Si at 400 °C. A linear fit to the data indidicates an average GPC of 1.62 Å per cycle and a nucleation delay of ~15 cycles (from the *y*-intercept).

(100–400 °C).[31] While the present thermal process is competitive in terms of GPC, outperforming many conventional thermal routes such as $Ga(acac)_3$ and water (0.25–0.55 Å per cycle),[17] a plasma ALD variant could broaden the applicability of $Ga(triaz)_3$ by lowering the deposition temperature.

The measured thickness of Ga_2O_3 thin films deposited on Si substrates at 400 °C as a function of the number of cycles is shown in Fig. 4. A linear regression of the data yields a GPC of 1.62 Å per cycle, which is somewhat higher than the results in Fig. 2 but still within experimental error. The extrapolated intercept suggests a nucleation delay of ~15 cycles. This nucleation delay is comparable to our ALD study of GaN using $Ga(triaz)_3$ and NH_3 plasma, where delays of 16–21 cycles were observed depending on temperature.[22] Since the triazenide ligand system gives very similar nucleation delays for both GaN and Ga_2O_3 deposition, we speculate that the nucleation delay is caused by steric effects from the triazenide ligand system. In contrast, processes employing $Ga(O^iPr)_3$ and water[18] and $Ga(CH_3)_3$ and O_3,[32] typically show minimal or no measurable nucleation delay on Si or sapphire substrates.

3.2. Elemental composition

Elemental composition was determined by ToF-ERDA for several films deposited within the ALD temperature interval, using identical pulse-purge sequences while varying the deposition temperature and cycle count. Average atomic compositions before and after air annealing are listed in Table 1.

Ga and O were the major constituents in all films, whereas H, C, N, Cl, and Cu were detected at low levels. Cl likely originates from residual $Ga(triaz)_2Cl$ formed due to incomplete conversion of $GaCl_3$ to $Ga(triaz)_3$ during synthesis, while N, C, and H are consistent with fragments derived from the triazenide ligand. The presence of Cu is attributed to the mounting wire used to secure the substrate during deposition and subsequent annealing. Annealing significantly reduced impurity concentrations: H, C, N, and Cl decreased, while the O:Ga atomic ratio increased from ~1.4–1.6 in as-deposited films to ~1.6–1.7 after annealing, suggesting a slight shift toward O-rich compositions. The consistency of O : Ga ratios across samples underscores the reproducibility of the ALD process, despite variations in deposition temperature. A single outlier, the film deposited at 400 °C, showed elevated Cu content (rising from 1.6 to 4.9 at%), likely due to contamination from the mounting wire. We would here like to point out that the material quality of the films is too low to allow any meaningful analysis of detailed materials properties, such as point defects (vacancies and interstitials) commonly found in semiconductor materials.

Compared to previous studies, the films in this work show impurity profiles similar to those typically observed in thermal ALD processes using conventional Ga precursors combined with mild O-sources. By contrast, plasma ALD methods employing Ga cyclopentadienyls,[30] β-diketonates,[17] or trialkyl precursors[32] achieve cleaner films, owing to more efficient ligand elimination by energetic species.

3.3. Crystallinity and morphology

The GI-XRD patterns of the as-deposited and annealed Ga_2O_3 thin films are shown in Fig. 5. The films were annealed at 700 °C for 2 h in either N_2 or ambient air atmosphere. The as-deposited films were amorphous, while annealing induced crystallization to single-phase, polycrystalline monoclinic β-Ga_2O_3. The main diffraction peaks of the annealed samples are in agreement with the reference pattern (ICSD card No. 01-082-3838; lattice constants a = 12.21 Å, b = 3.04 Å, c = 5.80 Å) and align with literature on monoclinic β-Ga_2O_3.[29,33,34] The strong (111) reflection observed at ~35.6° under both annealing conditions corresponds to the primary peak reported in the β-Ga_2O_3 reference pattern, indicating that its high intensity reflects the intrinsic crystallography rather than an annealing atmosphere induced preferred orientation. The sharper, more

Table 1 ToF-ERDA atomic compositions of Ga_2O_3 films before and after annealing at 700 °C for 2 h in air

Deposition Temperature (°C)	Elemental composition before and after annealing (at%)															
	Ga		O		H		C		N		Cl		Cu		O:Ga	
	Before	After	Before	After	Before	After	Before	After	Before	After	Before	After	Before	After	Before	After
400	35.8	34.1	56.4	57.3	1.9	1.7	2.8	1.3	0.8	0.3	0.7	0.3	1.6	4.9	1.6	1.7
410	35.6	37.0	53.6	59.8	3.0	1.8	3.5	0.6	0.7	0.1	2.0	0.1	1.6	0.6	1.5	1.6
415	37.0	36.3	52.6	60.8	4.7	1.3	2.4	0.7	1.0	0.3	1.3	0.2	0.9	0.5	1.4	1.7

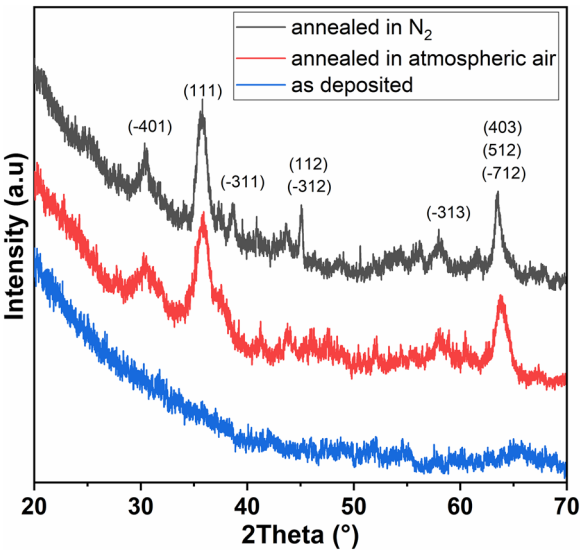

Fig. 5 GI-XRD patterns of Ga_2O_3 films: as-deposited (blue), annealed in ambient air (red), and annealed in N_2 (black), all at 700 °C for 2 h. Sharp diffraction peaks confirm crystallization to monoclinic β-Ga_2O_3; a strong (111) reflection at ~35.6° is observed under both annealing conditions.

intense peaks observed in the N_2-annealed film indicate a higher degree of crystallinity, potentially due to larger grain size or suppressed O-driven defect formation in the inert environment.

The surface morphology of Ga_2O_3 films, both as-deposited and annealed, was examined using SEM to assess textural features, porosity, and grain evolution (Fig. 6). Notably, these are the same samples analysed by GI-XRD. As-deposited films exhibit a disordered, cluster-like morphology with voids and poorly connected regions. This porous appearance is characteristic of amorphous ALD films grown at low temperatures, where limited adatom mobility produces an open microstructure and elevated surface roughness.

Upon annealing at 700 °C for 2 h, clear differences emerge between films treated in N_2 and ambient air. The N_2-annealed sample shows moderate grain coarsening and partial densification, consistent with suppression of oxidative surface reactions that can otherwise promote grain-boundary healing. By contrast, the air-annealed film appears more continuous and compact. High magnification images reveal tightly packed, well-defined grains with reduced porosity. This improved microstructure is consistent with thermally activated diffusion and recrystallization aided by the O-rich environment. The oxidizing environment likely reduces grain-boundaries defects, enabling larger grain growth and a denser film.

3.4. Optical and electrical properties

The optical transmittance spectra of Ga_2O_3 films deposited at 400 °C with 10 and 4 s water pulses are shown in Fig. 7. Both as-deposited and post-annealed states were measured and normalized against a bare glass substrate. The bare substrate showed a maximum transmittance of 91.2%, which was set to 100% for comparison. Relative to this baseline, as-deposited films maintained highly transparent, with normalized transmittance values of 96.5–97.1%. After annealing, transmittance decreased to 87.6–90.7% (Table 2). This trend is expected, as amorphous films generally have fewer grain boundaries that scatter or absorb light, whereas crystallization introduces grain-boundary scattering, defect absorption, and often higher density, all of which reduce transmittance.[35] Reducing the water pulse from 10 s to 4 s did not significantly affect the optical transmittance in the as-deposited films, indicating that within the amorphous phase excess water does not substantially alter optical properties. Upon annealing, both samples showed a similar ~10% decrease in transmittance, suggesting that the change is dominated by morphological evolution rather than compositional differences. A secondary contributor to the post-anneal reduction may be handling related contamination, *e.g.*, residues from adhesive tape used during the measurements.

The Tauc plots reveal a shift of the absorption edge to higher energy after annealing (Fig. 8). In the as-deposited state, the optical bandgaps are 3.74 eV (10 s water) and 3.77 eV (4 s water), with linear-fit R^2 values of 0.9915 and 0.9920, respectively. After annealing at 500 °C for 4 h in ambient air, the extrapolated bandgaps increase to 3.98 eV and 4.00 eV (R^2 = 0.9938 and 0.9980). Thus, annealing increases the apparent bandgap by 0.24 eV, consistent with structural and compositional changes. Here it should be noted that these band gap values are for a very thin film and not bulk material.

Based on XRD and ToF-ERDA (Fig. 5 and Table 1), annealing promotes nucleation of crystalline domains, reduces impurities, and increases the O:Ga ratio from ~1.4–1.6 to ~1.6–1.7. These changes are expected to reduce sub-gap absorption by decreasing tail states associated with defects and to improve short-range order *via* more regular Ga–O bonding. Both effects likely contribute to the observed increase in optical bandgap. Although the annealed films are "O-rich" (O:Ga > 1.5), this does not imply complete elimination of O-vacancies. Residual vacancies may persist, and –OH or interstitial O species may be present. Thus, the modest bandgap increase reflects partial defect healing and early-stage crystallization rather than a transition to fully stoichiometric β-Ga_2O_3. These observations align with prior reports: Lim *et al.* found a larger bandgap increase (0.65 eV) only after full recrystallization at 600 °C,[36] and first-principles calculations by Peelaers and Van de Walle showed that removing donor-like O-vacancies and C-related defects progressively widens the bandgap toward the ~4.8 eV limit of bulk β-Ga_2O_3.[37,38] The modest shift observed here is therefore consistent with partial crystallization and intermediate defect densities at 500 °C.

The electrical properties of the Ga_2O_3 thin films before and after annealing are summarized in Table 3. Conductivity was calculated using four-point-probe sheet resistance and film thickness obtained by XRR.

The as-deposited films exhibit moderate conductivity, 2.6–3.1 mS cm^{-1}. Here we also measured films deposited at 400 °C with both 4 s and 10 s water pulses and could not see any difference in their conductivity, within experimental error. After annealing at 700 °C, conductivity increased in all

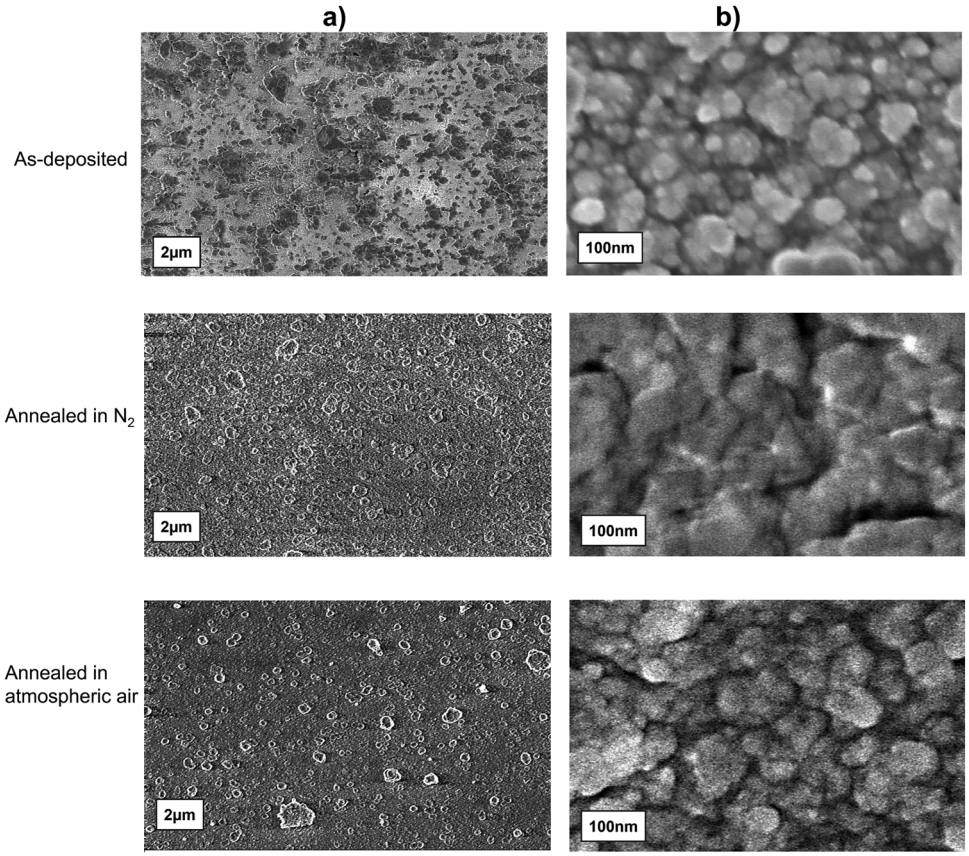

Fig. 6 SEM micrographs of Ga_2O_3 films: as-deposited (top); annealed in N_2 (middle); annealed in ambient air (bottom). (a) Left column: low-magnification images; (b) right column: high-magnification images. Air-annealed films appear denser with more uniform grains.

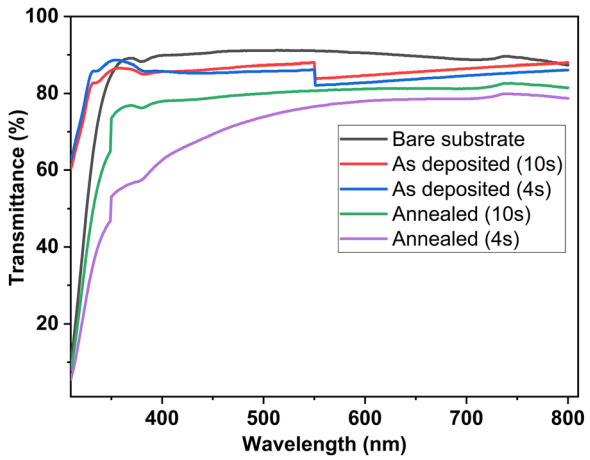

Fig. 7 Spectral transmittance of Ga_2O_3 films on glass, shown for as-deposited and annealed states. As-deposited films exhibit higher optical transparency than their annealed counterparts.

Table 2 Maximum transmittance of Ga_2O_3 films, reported as measured values and as values normalized to the bare substrate (91.2%). Both samples show a ~10% decrease in transmittance after annealing

Sample	Measured (%)	Normalized (%)
Bare substrate	91.2	100
10 s water pulse (as-deposited)	88.0	96.5
4 s water pulse (as-deposited)	88.6	97.1
10 s water pulse (annealed)	82.7	90.7
4 s water pulse (annealed)	79.9	87.6

measured samples. For example, the film deposited at 415 °C shows a 10-fold rise from 3.11 to 32.8 mS cm^{-1}, despite a drop in Cu from 1.6 to 0.6 at%. This improvement is attributed primarily to enhanced crystallinity and a more stoichiometric O : Ga ratio (1.5 to 1.6), which together reduce defect scattering and increase carrier mobility. Although shallow donors, such as residual H and C, can contribute to n-type conductivity in Ga_2O_3, their concentrations decrease after annealing. Thus, the conductivity enhancement is more plausible due to improved transport in a more ordered microstructure rather than an increase in donor density. The film deposited at 410 °C exhibits a similar trend, with conductivity rising 4-fold from 2.60 to 10.6 mS cm^{-1}, consistent with the same mechanism. By contrast, the film deposited at 400 °C behaves anomalously. Its conductivity increased by more than 360-fold from 2.90×10^{-3} to 1.05 S cm^{-1}, far exceeding what crystallinity and stoichiometry alone would explain. This behaviour coincides with a substantial rise in Cu from 1.6 to 4.9 at% (Table 1). At this elevated concentration, the Cu-related phases (*e.g.* Cu_2O or

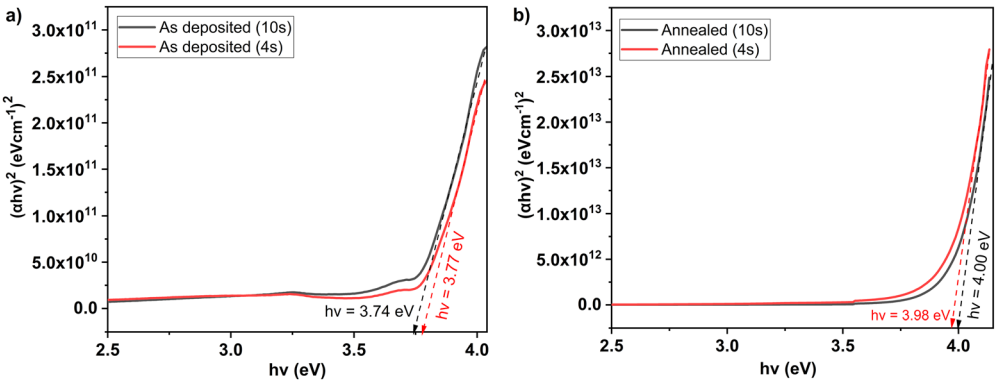

Fig. 8 Tauc plots for Ga_2O_3 films on glass deposited with 10 s and 4 s water pulses: (a) as-deposited; (b) annealed at 500 °C for 4 h in ambient air. Bandgaps were extracted by linear extrapolation of the near-edge region to the energy axis. Annealing shifts the absorption edge to higher energy, increasing the apparent bandgap.

Table 3 Electrical properties of Ga_2O_3 thin films before and after annealing. Conductivity was calculated from four-point probe sheet resistance and XRR thickness. The sample deposited at 400 °C shows anomalously high post-anneal conductivity, attributed to elevated Cu contamination

Deposition temperature (°C)	Sheet resistance (MΩ □$^{-1}$)		Thickness (nm)	Conductivity (S cm^{-1})	
	As-deposited	Annealed		As-deposited	Annealed
400	78.54	0.216	44	2.90×10^{-3}	1.05
410	93.52	22.87	41.1	2.60×10^{-3}	1.06×10^{-2}
415	77.68	7.39	41.3	3.11×10^{-3}	3.28×10^{-2}

metallic Cu) could form conductive inclusions or percolative pathways that dominate the electrical response. We would like to point out that we regard this as an anomality and while crystallization and residual donors may still play a role, the exceptionally high conductivity in this film is most consistent with Cu-mediated conduction.

4. Conclusions

This work demonstrates ALD of Ga_2O_3 using $Ga(triaz)_3$ with water. Saturation behaviour was observed with precursor pulse durations ≥2 s, yielding a GPC of ∼1.5 Å. The process exhibited a narrow ALD temperature interval between 400 and 415 °C, and film thickness scaled linearly with cycle count after a ∼15 cycles nucleation delay. $Ga(triaz)_3$ showed reactivity comparable to Ga trialkyl, halide, and alkoxide precursors used in conventional thermal ALD. As-deposited films were near-stoichiometric but contained minor C, H, N, and Cl (precursor derived), and Cu from hardware. Annealing reduced these impurities and increased the O : Ga ratio to ∼1.6–1.7. Cl levels remained minimal throughout, highlighting the effectiveness of precursor purification and ligand design. As a result, the films produced here rank among the purest reported for thermal ALD of Ga_2O_3 using water as the O-source. GI-XRD confirmed amorphous as-deposited films crystallized to monoclinic β-Ga_2O_3 after annealing at 700 °C. Optically, transmittance exceeded 96% in the as-deposited state and decreased by ∼10% after annealing, and Tauc plots showed the bandgap increasing from ∼3.74 to 4.00 eV. Electrically, all films exhibit higher conductivity after annealing, consistent with β-phase formation and improved structural order. Taken together, XRD and ToF-ERDA corroborated that the property changes arised from crystallization, reduced defect/ligand residues, and a modest shift toward O-richer composition.

Conflicts of interest

The authors declare no conflict of interest.

Data availability

The data that support the findings of this study are available from the corresponding author upon a reasonable request.

Acknowledgements

The Swedish foundation for Strategic Research through the project ''Time-resolved low temperature CVD for III-nitrides'' (SSF-RMA 15-0018) is gratefully acknowledged for financial support. HP acknowledges financial support from the Swedish Government Strategic Research Area in Materials Science on Advanced Functional Materials at Linköping University (Faculty Grant SFO-Mat-LiU No. 2009-00971). KS acknowledges financial support by the Swedish Research Council (Grant No. VR-2021-04113) and the Åforsk foundation (Grant No. 22-150). PSM acknowledges personal financial support from his family during his MSc studies.

References

1 A. R. Hefner, R. Singh, J.-S. Lai, D. W. Berning, S. Bouche and C. Chapuy, *IEEE Trans. Power Electron.*, 2001, **16**, 273–280.
2 F. Iucolano and T. Boles, *Mater. Sci. Semicond. Process.*, 2019, **98**, 100–105.
3 J. Zhang, P. Dong, K. Dang, Y. Zhang, Q. Yan, H. Xiang, J. Su, Z. Liu, M. Si, J. Gao, M. Kong, H. Zhou and Y. Hao, *Nat. Commun.*, 2022, **13**, 3900.
4 M. H. Wong, O. Bierwagen, R. J. Kaplar and H. Umezawa, *J. Mater. Res.*, 2021, **36**, 4601–4615.
5 A. E. Islam, N. P. Sepelak, K. J. Liddy, R. Kahler, J. Williams, D. M. Dryden, A. J. Green and K. D. Chabak, *IMAP Proc.*, 2022, 58–62.
6 T. Moule, S. Dalcanale, A. S. Kumar, M. J. Uren, W. Li, K. Nomoto, D. Jena, H. G. Xing and M. Kuball, *IEEE Trans. Electron Devices*, 2022, **69**, 75–81.
7 S. J. Pearton, J. Yang, P. H. Cary, F. Ren, J. Kim, M. J. Tadjer and M. A. Mastro, *Appl. Phys. Rev*, 2018, **5**, 011301.
8 J. W. Roberts, P. R. Chalker, B. Ding, R. A. Oliver, J. T. Gibbon, L. A. H. Jones, V. R. Dhanak, L. J. Phillips, J. D. Major and F. C.-P. Massabuau, *J. Cryst. Growth*, 2019, **528**, 125254.
9 Z. Zhang, P. Yan, Q. Song, H. Chen, W. Zhang, H. Yuan, F. Du, D. Liu, D. Chen and Y. Zhang, *Fundam. Res.*, 2024, **4**, 1292–1305.
10 F. Mezzadri, G. Calestani, F. Boschi, D. Delmonte, M. Bosi and R. Fornari, *Inorg. Chem.*, 2016, **55**, 12079–12084.
11 R. Clark, K. Tapily, K.-H. Yu, T. Hakamata, S. Consiglio, D. O'Meara, C. Wajda, J. Smith and G. Leusink, *APL Mater.*, 2018, **6**, 058203.
12 H. Pedersen and S. D. Elliott, *Theor. Chem. Acc.*, 2014, **133**, 1476.
13 S. M. George, *Chem. Rev.*, 2010, **110**, 111–131.
14 C. Hou, K. Liang, Z. Yang, Q. Wang, Y. Zhang and F. Chen, *J. Cryst. Growth*, 2025, **650**, 127974.
15 Z. Qi, S. An, L. Jiang and Y. Cao, *Opt. Express*, 2025, **33**, 25397.
16 C. L. Dezelah, J. Niinistö, K. Arstila, L. Niinistö and C. H. Winter, *Chem. Mater.*, 2006, **18**, 471–475.
17 M. Nieminen, L. Niinistö and E. Rauhala, *J. Mater. Chem.*, 1996, **6**, 27–31.
18 D. Choi, K.-B. Chung and J.-S. Park, *Thin Solid Films*, 2013, **546**, 31–34.
19 H. Lee, K. Kim, J. Woo, D. Jun, Y. Park, Y. Kim, H. W. Lee, Y. J. Cho and H. M. Cho, *Chem. Vap. Deposition*, 2011, **17**, 191–197.
20 N. J. O'Brien and H. Pedersen, *Dalton Trans.*, 2025, **54**, 2709–2717.
21 N. J. O'Brien, P. Rouf, R. Samii, K. Rönnby, S. C. Buttera, C.-W. Hsu, I. G. Ivanov, V. Kessler, L. Ojamäe and H. Pedersen, *Chem. Mater.*, 2020, **32**, 4481–4489.
22 P. Rouf, R. Samii, K. Rönnby, B. Bakhit, S. C. Buttera, I. Martinovic, L. Ojamäe, C. Hsu, J. Palisaitis, V. Kessler, H. Pedersen and N. J. O'Brien, *Chem. Mater.*, 2021, **33**, 3266–3275.
23 P. Rouf, J. Palisaitis, B. Bakhit, N. J. O'Brien and H. Pedersen, *J. Mater. Chem. C*, 2021, **9**, 13077–13080.
24 P. Mpofu, P. Rouf, N. J. O'Brien, U. Forsberg and H. Pedersen, *Dalton Trans.*, 2022, **51**, 4712–4719.
25 R. Samii, S. C. Buttera, V. Kessler and N. J. O'Brien, *Eur. J. Inorg. Chem.*, 2022, e202200161.
26 J. Jokinen, J. Keinonen, P. Tikkanen, A. Kuronen, T. Ahlgren and K. Nordlund, *Nucl. Instrum. Methods Phys. Res., Sect. B*, 1996, **119**, 533–542.
27 J. F. Ziegler, M. D. Ziegler and J. P. Biersack, *Nucl. Instrum. Methods Phys. Res., Sect. B*, 2010, **268**, 1818–1823.
28 'X'Pert Reflectivity Software, Version 1.3, PANalytical B. V.
29 R. O'Donoghue, J. Rechmann, M. Aghaee, D. Rogalla, H.-W. Becker, M. Creatore, A. D. Wieck and A. Devi, *Dalton Trans.*, 2017, **46**, 16551–16561.
30 F. Mizutani, S. Higashi, M. Inoue and T. Nabatame, *J. Vac. Sci. Technol., A*, 2020, **38**, 02241.
31 I. Donmez, C. Ozgit-Akgun and N. Biyikli, *J. Vac. Sci. Technol., A*, 2013, **31**, 01A110.
32 D. J. Comstock and J. W. Elam, *Chem. Mater.*, 2012, **24**, 4011–4018.
33 F. Shi and H. Qiao, *J. Mater. Sci.: Mater. Electron.*, 2020, **31**, 20223–20231.
34 X. Wang, H. Qiao, T. Liu, F. Song, Z. An, Y. Xu, L. Zhang and F. Shi, *J. Mater. Sci.: Mater. Electron.*, 2022, **33**, 13040–13050.
35 N. Makeswaran, A. K. Battu, E. Deemer and C. V. Ramana, *Cryst. Growth Des.*, 2020, **20**, 2893–2903.
36 H. Lim, D. Kim, S. Yeon Cha, B. Simon Mun, D. Young Noh and H. Chol Kang, *Appl. Surf. Sci.*, 2022, **585**, 152771.
37 H. Peelaers and C. G. Van de Walle, *Phys. Status Solidi*, 2015, **252**, 828–832.
38 H. Peelaers and C. G. Van de Walle, *Phys. Rev. B*, 2017, **96**, 081409.